



# Graphene-Assisted Growth of Patterned Perovskite Films for Sensitive Light Detector and Optical Image Sensor Application

Chun-Yan Wu, Zhenyu Wang, Lin Liang, Tijun Gui, Wei Zhong, Rui-Chao Du, Chao Xie,\*  
Li Wang, and Lin-Bao Luo\*

Controlled growth of high-quality patterned perovskite films on a large scale is essentially required for the application of this class of materials in functional integrated devices and systems. Herein, graphene-assisted hydrophilic–hydrophobic surface-induced growth of Cs-doped FAPbI<sub>3</sub> perovskite films with well-patterned shapes by a one-step spin-coating process is developed. Such a facile fabrication technique is compatible with a range of spin-coated perovskite materials, perovskite manufacturing processes, and substrates. By employing this growing method, controllable perovskite photodetector arrays are realized, which have not only prominent photoresponse properties with a responsivity and specific detectivity of 4.8 AW<sup>-1</sup> and 4.2 × 10<sup>12</sup> Jones, respectively, but also relatively small pixel-to-pixel variation. Moreover, the photodetectors array can function as an effective visible light image sensor with a decent spatial resolution. Holding the above merits, the proposed technique provides a convenient and effective pathway for large-scale preparation of patterned perovskite films for multifunctional application purposes.

of individual optoelectronic units composed of bulk polycrystalline thin films or single crystals of perovskite materials.<sup>[11–14]</sup> From the view of many practical applications, development of optoelectronic device arrays are essential for diverse integrated optoelectronic devices and systems, which requires controllable and precise growth of high-quality patterned perovskite materials with designed shapes.<sup>[15,16]</sup> The conventional photolithography process is the most extensively employed and useful technique for micropatterning of functional materials in the current semiconductor industry.<sup>[17]</sup> However, the direct application of this technique for patterning perovskite materials has been ruled out because of the solubility of perovskites in many polar and protic solvents and the sensitivity of the organic component in perovskites.<sup>[18,19]</sup>

## 1. Introduction

In recent years, due to their rich physical and optoelectronic properties (e.g., tunable bandgap, large optical absorption coefficient, long charge carrier diffusion length, easy processibility, etc.),<sup>[1]</sup> organic–inorganic hybrid perovskites have emerged as a promising class of candidate materials for a variety of optoelectronic applications including solar cells,<sup>[2–4]</sup> photodetectors,<sup>[5–7]</sup> light-emitting diodes,<sup>[8,9]</sup> and lasers.<sup>[10]</sup> Currently, the majority of studies have been focused on the development

To circumvent the above dilemma, a number of methods have been developed recently. For example, large-scale parallel aligned perovskite micro/nanowire arrays or vertically standing perovskite nanowire arrays have been successfully realized through self-assembly of perovskite precursors assisted by techniques such as blade-coating,<sup>[20,21]</sup> periodical geometrical confinement,<sup>[22–24]</sup> or periodical template guiding.<sup>[25–27]</sup> However, it is rather difficult to precisely control the crystal shape using these methods, which limits the advance in integrated devices and systems. In addition, wafer-scale preparation of perovskite microplate crystals has also been realized through some methods including vapor-phase conversion,<sup>[28]</sup> chemical vapor deposition (CVD) growth,<sup>[29]</sup> or wettability-mediated template method.<sup>[30]</sup> Nevertheless, homogenous prepatterned seed layers or complex templates are always required, which needs expensive apparatuses and renders the fabrication process extremely complicated and costly. What is more, the involvement of high temperature or unusual substrates also makes these techniques not applicable for use in applications like flexible and deformable optoelectronic devices. On the other hand, solution-processed spin-coating technique at relatively mild reaction condition has proven to be an effective way for preparing high-quality perovskite films toward high-performance and cost-effective optoelectronics. Very recently, by utilizing the wetting/dewetting behavior of perovskite precursor solutions

Prof. C. Y. Wu, Z. Wang, T. Gui, W. Zhong, R. C. Du, Dr. C. Xie,  
L. Wang, Prof. L. B. Luo  
School of Electronic Science and Applied Physics  
Hefei University of Technology  
Hefei, Anhui 230009, China  
E-mail: chaoxie@hfut.edu.cn; luolb@hfut.edu.cn

L. Liang  
School of Material Science and Engineering and Anhui Provincial Key  
Laboratory of Advanced Functional Materials and Devices  
Hefei University of Technology  
Hefei, Anhui 230009, China

The ORCID identification number(s) for the author(s) of this article can be found under <https://doi.org/10.1002/smll.201900730>.

DOI: 10.1002/smll.201900730

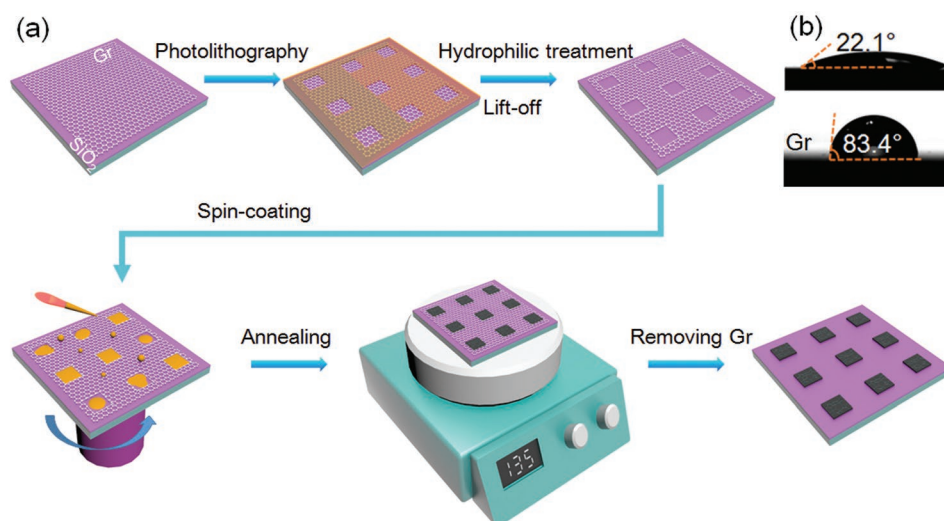


**Figure 1.** a) Schematic illustration of the procedures for preparing patterned perovskite films. b) Contact angles of the perovskite precursor on graphene (bottom panel) and an oxygen plasma-treated  $\text{SiO}_2/\text{Si}$  substrate (top panel), respectively.

on hydrophilic/hydrophobic surface produced by photolithography prepatterned organic self-assembly monolayers (SAMs) or polymer layers, several groups have achieved the deposition of patterned perovskite films with designed shapes on rigid or flexible substrates via spin-coating technique.<sup>[31–33]</sup> Based on these techniques, high-performance optoelectronic devices like semitransparent perovskite solar cells, ultrathin perovskite-on-Si multiplexed image sensor arrays, and flexible perovskite photodetector arrays have also been demonstrated. In spite of these exciting progresses, some inevitable limitations still exist in the above-mentioned techniques. For example, normally, high-quality and continuous organic SAMs can only be successfully modified onto some special substrates, which restricts the vast applications of the techniques. Also, the processes of modification of organic SAMs and removal of residual polymer layers often involve the use of toxic organic solvents, making these techniques environmental unfriendly.

Inspired by the above studies, we herein put forward a hydrophilic/hydrophobic surface-induced large-scale growth of high-quality patterned Cs-doped  $\text{FAPbI}_3$  perovskite films with high yield through one-step spin-coating process assisted by CVD-grown graphene films. As we all know, CVD-graphene possesses a natural hydrophobic surface due to airborne contaminants and moisture adsorption,<sup>[34]</sup> and it can also be transferred onto arbitrary substrates in principle.<sup>[35]</sup> Therefore, the proposed technique is compatible not only with a variety of spin-coated perovskite materials and perovskite manufacturing process but also with many substrates enabling some specific applications like next-generation flexible and deformable optoelectronics. With this technique, we obtained  $6 \times 6$  perovskite photodetector arrays, which display good photoresponse characteristics in terms of decent responsivity and specific detectivity of  $4.8 \text{ AW}^{-1}$  and  $4.2 \times 10^{12}$  Jones, with narrow pixel-to-pixel deviation. Furthermore, it is found that these photodetector arrays can work as a visible light image sensor, exhibiting a reasonable spatial resolution. Considering the above good results along with the well-developed graphene

processing technologies, it is believed that the proposed technique opens up a simple, reliable, and cost-effective avenue for large-scale growth of patterned perovskite films for functional integrated device and system applications.

## 2. Results and Discussion

**Figure 1a** shows the schematic illustration of the procedures for preparing patterned perovskite films. First, a high-quality continuous CVD-grown graphene film was transferred onto a pre-cleaned  $\text{SiO}_2/\text{Si}$  substrate through a polymethyl methacrylate (PMMA)-assisted transfer method. After removing PMMA with acetone, a solution of positive photoresist was spin-coated onto the graphene layer to generate a photoresist layer, and a standard photolithography process was employed to define the photoresist with desired micropatterns. Afterward, the substrate was treated with oxygen plasma to selectively remove exposed graphene and render a hydrophilic surface within the region of the micropatterns. The residual photoresist was then removed by acetone, leaving graphene layer with duplicated micropatterns atop the substrate. Subsequently, a solution of  $\text{FA}_{0.85}\text{Cs}_{0.15}\text{PbI}_3$  perovskite precursors was spin-coated onto the substrate. During this process, the solution was prone to migrate to the hydrophilic region (oxygen plasma-treated oxide layer) due to the spontaneous dewetting property on the hydrophobic region (graphene layer), which was confirmed by a much larger contact angle of the solution on graphene layer ( $83.4^\circ$ ) than that on oxygen plasma-treated oxide layer ( $22.1^\circ$ ) (Figure 1b). Meanwhile, due to the centrifugal force of the spinning, the excess solution on graphene layer would be removed from the substrate. Finally, after thermal annealing and removal of graphene via another oxygen plasma treatment, a perovskite film with desired micropatterns was obtained on the substrate.

The quality of the as-prepared patterned perovskite films was then probed by performing morphological and structural characterizations. **Figure 2a–c** displays the field-emission

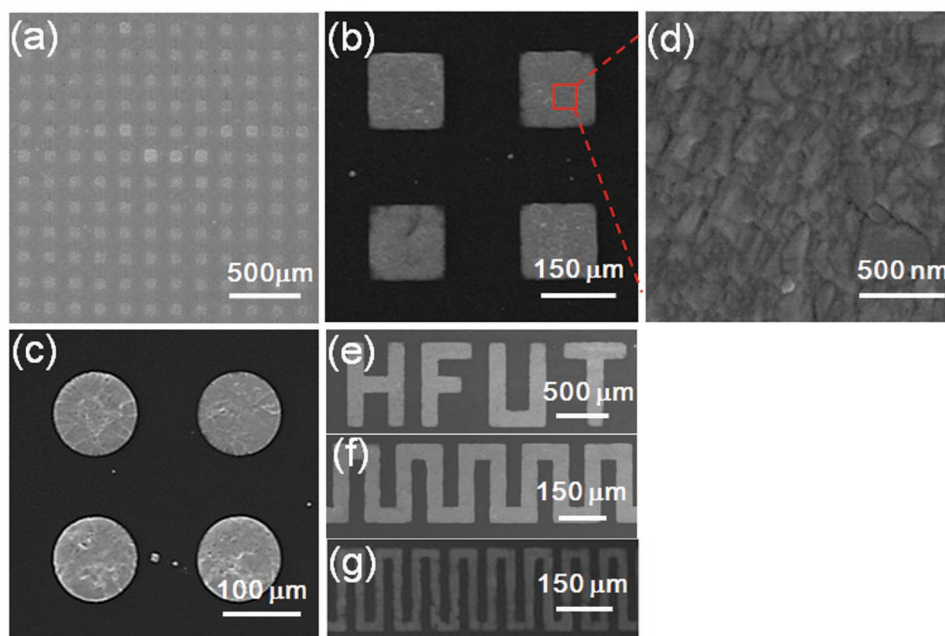


**Figure 2.** FESEM images of the perovskite films with the patterns of a,b) periodic square array and c) periodic round array, respectively. d) A magnified FESEM image of the patterned perovskite film. FESEM images of the perovskite films arranged in e) a HFUT pattern, a meander line with the width of f) 50  $\mu\text{m}$  and g) 25  $\mu\text{m}$ , respectively.

scanning electron microscopy (FESEM) images of perovskite films of periodic square and round array patterns with different magnifications. Obviously, the as-grown films had uniform and regular shapes with sharp edges, verifying the selective growth of the perovskite film on the substrate. We noted that there exist some undesired particles outside the patterned regions, which was likely due to the contaminants or cracks on graphene that can reduce the hydrophobicity of the underlying surface. Such a situation could be avoided by improving the graphene quality and optimizing graphene transfer processes in future work. Furthermore, from a magnified FESEM image plotted in Figure 2d, it was observed that the patterned perovskite film possessed compact and uniform surface with few pinholes and cracks, implying the homogenous growth of the perovskite within the hydrophilic region. Apart from periodic arrays, the proposed technique can be applied to prepare perovskite films with other micropatterns as well. Figure 2e–g presents an FESEM image of perovskite films arranged in an HFUT character. In addition, meander lines of perovskite films with widths of 50 and 25  $\mu\text{m}$ , respectively, have also been realized. As shown in Figure 2g, even with the space width of only 25  $\mu\text{m}$ , continuous lines of perovskite film with clear edges can still be realized. These results undoubtedly show that the present graphene-assisted patterned growth method holds a great possibility for fabrication of other materials for multifunctional purposes.

Besides the convenience to achieve various desired pattern, the graphene-assisted growth method can also allow us to obtain smooth perovskite film with a root mean square roughness of only  $\approx 9.71$  nm, as shown by a 3D atomic force microscopy (AFM) image scanned in a representative area of  $3 \times 3 \mu\text{m}^2$  (Figure 3a). Such roughness is close to that of standard perovskite layer without graphene ( $\approx 10.2$  nm, shown in Figure S2,

Supporting Information). Statistical analysis of the 36 patterned perovskite films in Figure 3b reveals that the thickness is in the range of 0.95–1.76  $\mu\text{m}$ , with an average value of  $\approx 1.3$   $\mu\text{m}$ , according to the cross-sectional FESEM image (Figure 3c). What is more, as depicted in Figure 3d, the diffraction peaks in the X-ray diffraction (XRD) pattern of the sample can be all assigned to the black phase of  $\text{FAPbI}_3$  perovskite, which coincides with that of  $\text{FA}_{0.85}\text{Cs}_{0.15}\text{PbI}_3$  perovskites in literatures,<sup>[36]</sup> and discloses the fine crystallinity of the as-prepared perovskite arrays via the one-step spin-coating method.

By using the above graphene-assisted growth technique, we then fabricated an optical image sensor composed of  $6 \times 6$  pixels perovskite thin film photodetector arrays. The detailed fabrication process is similar to the above-mentioned preparation procedures except for the use of a  $\text{SiO}_2/\text{Si}$  substrate with predefined Au parallel electrodes arrays, as schematically demonstrated in Figure S1 in the Supporting Information. Figure 4a shows an optical photography of the as-constructed perovskite photodetector arrays. For the convenience of electrical characterization, the substrate was fixed onto a printed circuit board (PCB). Notably, as confirmed by the FESEM image of an individual device (inset in Figure 4a), continuous and compact perovskite films were formed within a  $300 \times 300 \mu\text{m}^2$  area across the device channel, which is favorable for achieving a good photo-response performance. Figure 4b shows the current–voltage ( $I$ – $V$ ) characteristics of a representative pixel device in dark and under white light illumination ( $1.25 \text{ mW cm}^{-2}$ ), respectively. At a bias voltage of 3 V, the device displayed a low dark current of only 0.67 nA. Interestingly, upon irradiation, the channel current increased drastically to as high as 27.71 nA, revealing a high sensitivity of the device to incident illumination. Time-dependent photoresponse under periodically switched

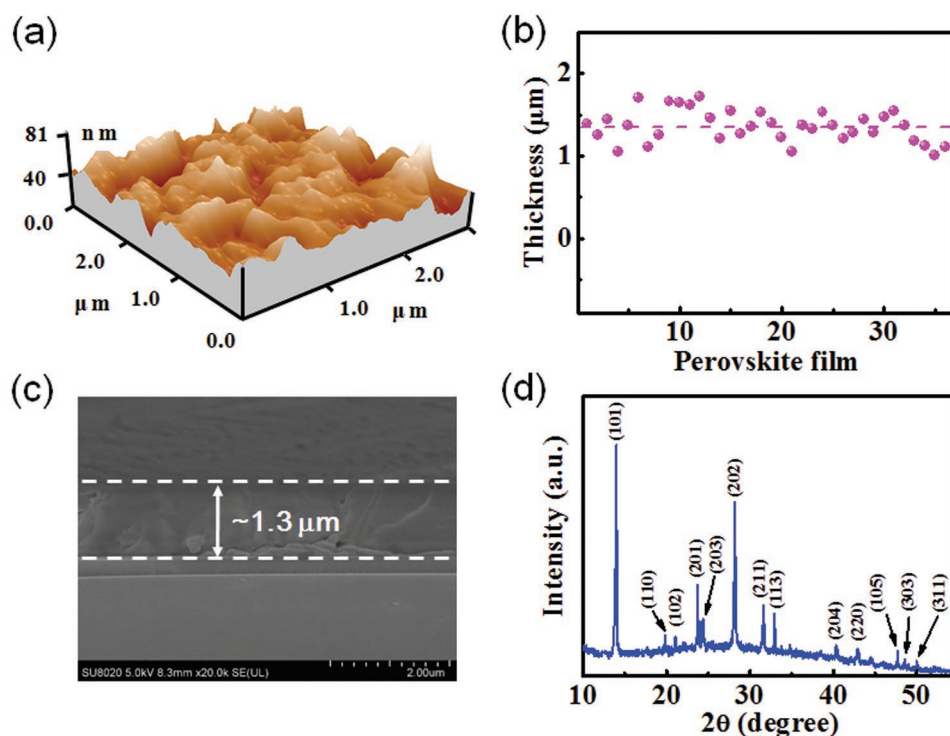


**Figure 3.** a) 3D morphology of the AFM image. b) Thickness distribution of the perovskite thin film. c) Cross-section FESEM image of the perovskite thin film. d) XRD pattern of the as-fabricated patterned  $\text{FA}_{0.85}\text{Cs}_{0.15}\text{PbI}_3$  perovskite film.

white light illumination was also investigated. As depicted in Figure 4c, the detector responded steadily and repeatedly to the incident irradiation, giving a relatively large  $I_{\text{light}}/I_{\text{dark}}$  ratio of  $\approx 10^2$  at 1 V bias voltage.

The photoresponse of the device depended strongly on the intensity of the incident light. Figure 4d displays the  $I$ - $V$  curves under white light illumination with varied intensities. Apparently, the channel current increased monotonously from 2.54 to 45.2 nA when changing the light intensity from  $37.6 \mu\text{W cm}^{-2}$  to  $4.51 \text{ mW cm}^{-2}$  at 3 V bias voltage, which can be ascribed to the increased population of photoexcited charge carriers upon illumination with a stronger light intensity. In addition, the photocurrent curve as a function of light intensity can be well fitted by an extensively used power law:  $I \propto P^\theta$ , where the exponent  $\theta$  denotes an empirical value related to the recombination activity of photocarriers.<sup>[37]</sup> As shown in Figure 4e, fitting the curve rendered a  $\theta$  value of 0.59, which deviated significantly from the ideal value ( $\theta = 1$ ). Such a large deviation indicated the presence of strong recombination loss in the current perovskite photodetector, which was likely due to the carrier recombination occurred at abundant grain boundaries and surface trap states in the perovskite film.<sup>[38]</sup>

In order to quantitatively assess the device performance, two key performance parameters, responsivity ( $R$ ) and specific detectivity ( $D^*$ ) were calculated according to the following equations<sup>[39]</sup>

$$R = \frac{I_{\text{light}} - I_{\text{dark}}}{P_{\text{in}} S} \quad (1)$$

$$D^* = \frac{RS^{1/2}}{(2eI_{\text{d}})^{1/2}} \quad (2)$$

where  $I_{\text{light}}$  and  $I_{\text{dark}}$  represent channel current under illumination and in dark,  $P_{\text{in}}$  represents the incident light intensity,  $S$  represents the effective illuminating area ( $300 \times 10 \mu\text{m}^2$  here), and  $e$  represents the elementary charge, respectively. Based on the above equations,  $R$  and  $D^*$  were calculated to be  $1.2 \text{ AW}^{-1}$  and  $9.5 \times 10^{11} \text{ Jones (cmHz}^{1/2} \text{ W}^{-1})$ , respectively, at a light intensity of  $37.6 \mu\text{W cm}^{-2}$ . The  $R$  and  $D^*$  values were somewhat lower than those of a photodetector based on  $\text{FA}_{0.85}\text{Cs}_{0.15}\text{PbI}_3$  perovskite films prepared via the conventional one-step spin-coating method (at a white light intensity of  $0.6 \mu\text{W cm}^{-2}$ ),<sup>[36]</sup> which was probably caused by the following reasons. First, our patterned perovskite device had a much thicker perovskite active layer, which led to a larger dark current. In addition, the collection of photocarriers would be less effective in devices with bottom electrode contacts in comparison with those with top electrode contacts, considering that optical absorption taken place at the top side. Finally, as will be discussed later, light illumination with a lower intensity was more favorable for achieving a higher  $R$  and therefore a higher  $D^*$ . Figure 4f plots the dependence of  $R$  on the light intensity. Obviously, the  $R$  was negatively correlated with the light intensity, which further manifested the existence of strong recombination loss in the device. As a matter of fact, in such a photodetector, partial of photoexcited minority carriers are normally captured by sensitizing traps in the active layer, while photoexcited majority carriers transport across the channel to produce photocurrent.<sup>[39,40]</sup> Therefore, at a higher light intensity, saturation of sensitizing traps from minority carriers leads to intensified recombination activity of electrons and holes because of increased concentration of photocarriers.<sup>[41]</sup>

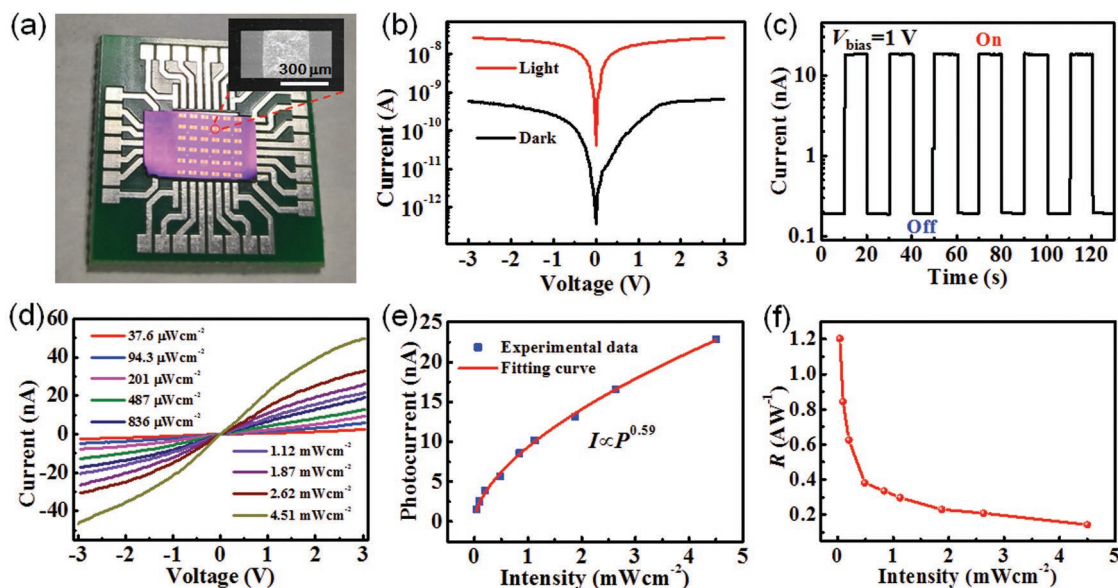


**Figure 4.** a) Optical photograph of a typical  $6 \times 6$  perovskite photodetector arrays fixed onto a printed circuit board (PCB), the inset shows an FESEM image of a single pixel device. b)  $I$ - $V$  curves of a typical perovskite photodetector in dark and under white light illumination ( $1.25 \text{ mW cm}^{-2}$ ) in the semi-logarithmic scale. c) Time-dependent photoresponse of the device at 1 V bias. d)  $I$ - $V$  characteristics of the device under white light illumination with different light intensities. e) Photocurrent as a function of the incident light intensity at 1 V bias. f) Responsivity as a function of the incident light intensity.

The above process is responsible for the decrease in  $R$  value with increasing light intensity.

To shed light on the dependence of device performance on incident light wavelength, the photoresponse of the perovskite photodetector under irradiation with different wavelengths was investigated. Figure 5a displays the  $I$ - $V$  curves under 405, 650, and 808 nm illuminations with a constant light intensity ( $100 \mu\text{W cm}^{-2}$ ). Significantly, the channel current was several

times higher upon 650 nm irradiation than those under 405 and 808 nm illuminations, implying that the device possessed the maximum sensitivity at around 650 nm. For all three wavelengths, the photocurrents were found to rise gradually with increasing light intensity, as shown in Figure 5b and Figures S2a and S3a in the Supporting Information. In addition, fitting the curves of photocurrent versus light intensity gave exponent  $\theta$  values of 0.68, 0.83, and 0.84 for light wavelengths of 405, 650,

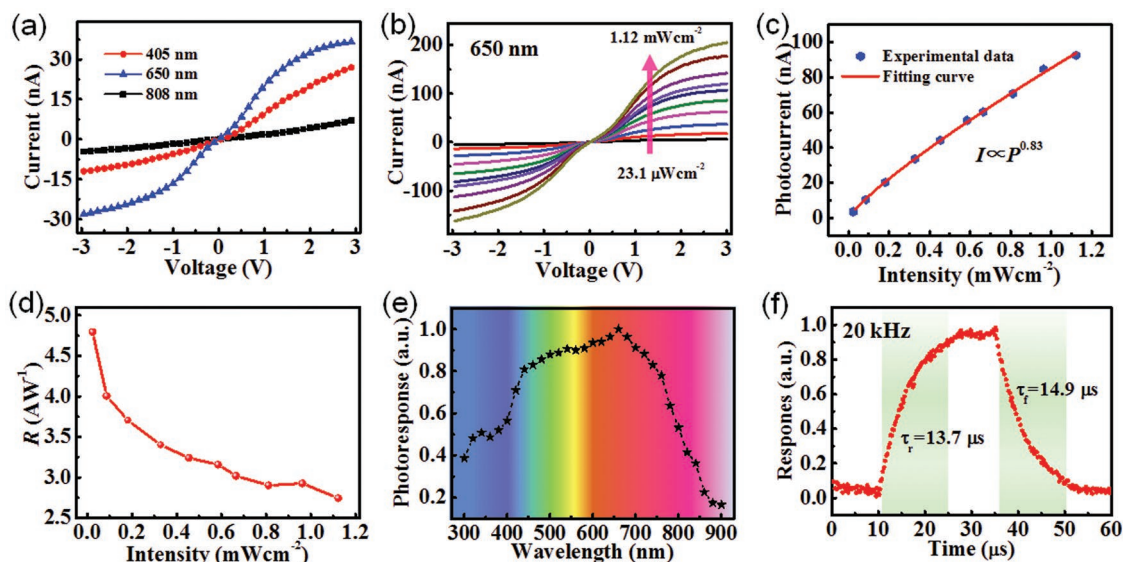


**Figure 5.**  $I$ - $V$  curves of the perovskite photodetector a) upon illuminations of different wavelengths, and b) under 650 nm illumination with varied light intensities. c) Photocurrent as a function of incident light intensity at 1 V bias. d) Responsivity as a function of incident light intensity. e) Spectral response of the device in the wavelength range from 300 to 900 nm. f) An individual photoresponse curve under the incident light with a frequency of 20 kHz.

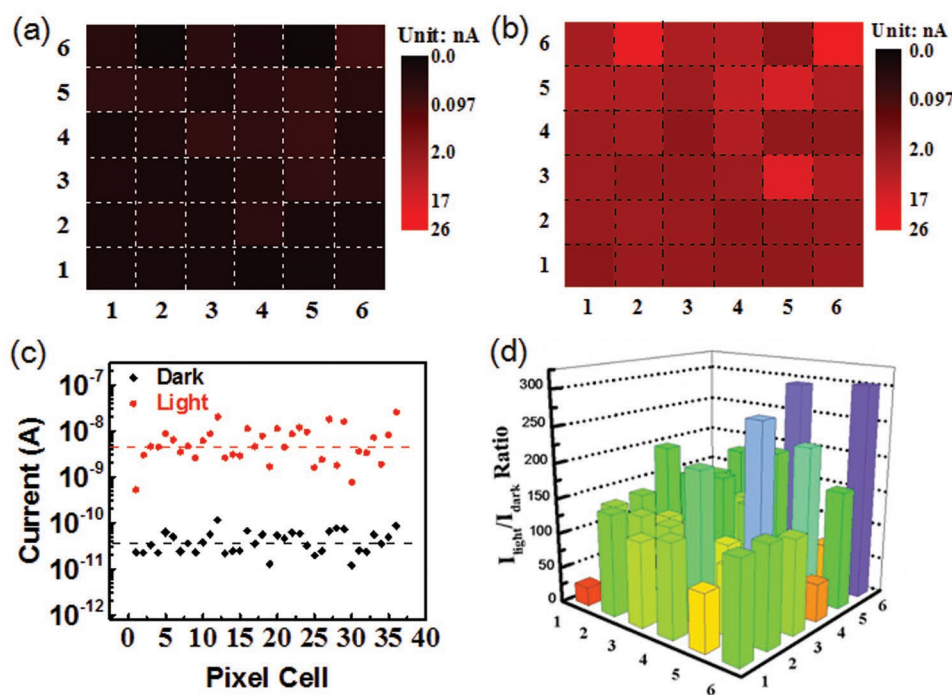


**Figure 6.** 2D contrast maps showing the channel current of the perovskite photodetector arrays a) in dark and b) upon a homogenous white light illumination. c) Channel current in dark and under light illumination for each pixel devices. The dash lines represent the average values for dark current (black) and photocurrent (red). d) A 3D diagram shows the  $I_{\text{light}}/I_{\text{dark}}$  ratio for each pixel device.

and 808 nm, respectively (Figure 5c and Figures S2b and S3b, Supporting Information). The obtained different  $\theta$  values suggest that there are some differences between processes of photocarrier generation and recombination in the device under varied light wavelengths.<sup>[42]</sup> Similarly, the  $R$  values declined monotonously with increasing light intensity as well (Figure 5d and Figures S2c and S3c, Supporting Information), and the maximum  $R$  and  $D^*$  were calculated to be  $4.8 \text{ AW}^{-1}$  and  $4.2 \times 10^{12}$  Jones, respectively, under 650 nm illumination with a light intensity of  $23.1 \mu\text{W cm}^{-2}$ . Figure 5e plots the spectral response of the device recorded at a fixed light intensity in the wavelength range of 300–900 nm. Clearly, the device displayed a broadband photoresponse with the maximum response located at the visible light region. The photoresponse declined rapidly at longer wavelength when the light wavelength exceeding  $\approx 760$  nm, which corresponded to the band-edge absorption of the  $\text{FA}_{0.85}\text{Cs}_{0.15}\text{PbI}_3$  perovskite.<sup>[36]</sup>

Response speed that reflects the ability of a photodetector to track fast-varying optical signal was also studied. Figure 5f plots an individual cycle of photoresponse curve of the detector under 650 nm illumination with a modulation frequency of 20 kHz. Clearly, the device can follow such a rapid optical signal with distinct on and off states, indicating a fast response speed of our device. Furthermore, the rise and decay times ( $\tau_r$  and  $\tau_f$ , defined as the duration needed for the photoresponse to rise (decay) from 10% (90%) to 90% (10%)) were estimated to be 13.7 and 14.9  $\mu\text{s}$ , respectively.<sup>[43]</sup> Such a rapid response speed is comparable with that of an ambipolar perovskite film phototransistor (6.5/5.0  $\mu\text{s}$ ),<sup>[44]</sup> and much faster than a perovskite network photodetector (0.3/0.4 ms) in previous studies.<sup>[45]</sup>

To verify the feasibility of the perovskite photodetector arrays for device integration purpose, the uniformity of photoresponse performance of all the  $6 \times 6$  pixel devices was further explored. Here, a homogenous white light irradiation ( $1.5 \text{ mW cm}^{-2}$ ) was used to illuminate the photodetector arrays, and the dark current and photocurrent of each pixel device were recorded separately. For ease of comparison, the results were summarized in the form of 2D contrast maps with varied colors denoting different current levels, as shown in Figure 6a,b. Apparently, all the detectors in the optical sensor can work properly. Careful analysis found that the majority of pixels had dark currents in the range of tens of picoamperes (pA) and photocurrents in the range of several nanoamperes (nA) at a 1 V bias voltage, indicating a closed photoresponse performance. The average dark current and photocurrent were found to be  $\approx 37.5 \text{ pA}$  and  $\approx 4.7 \text{ nA}$ , respectively (Figure 6c). Notably, although there was a pixel-to-pixel variation in device performance, the dark current and photocurrent held nearly the same deviation tendency from the average values for each pixel device. In other words, each pixel device had both higher or lower dark current and photocurrent in comparison with their respective average values. Such a phenomenon was probably ascribed to the fluctuation in the thickness of the patterned perovskite films in photodetector arrays. In addition, the  $I_{\text{light}}/I_{\text{dark}}$  ratio of all the pixel devices was extracted and plotted in Figure 6d. It is obvious that the majority of the devices exhibited a large  $I_{\text{light}}/I_{\text{dark}}$  ratio exceeding  $10^2$ , suggesting that the detected optical signal can be clearly distinguished from the background signal. Therefore, the present perovskite photodetector arrays possessed a huge potential for application as a visible light image sensor.

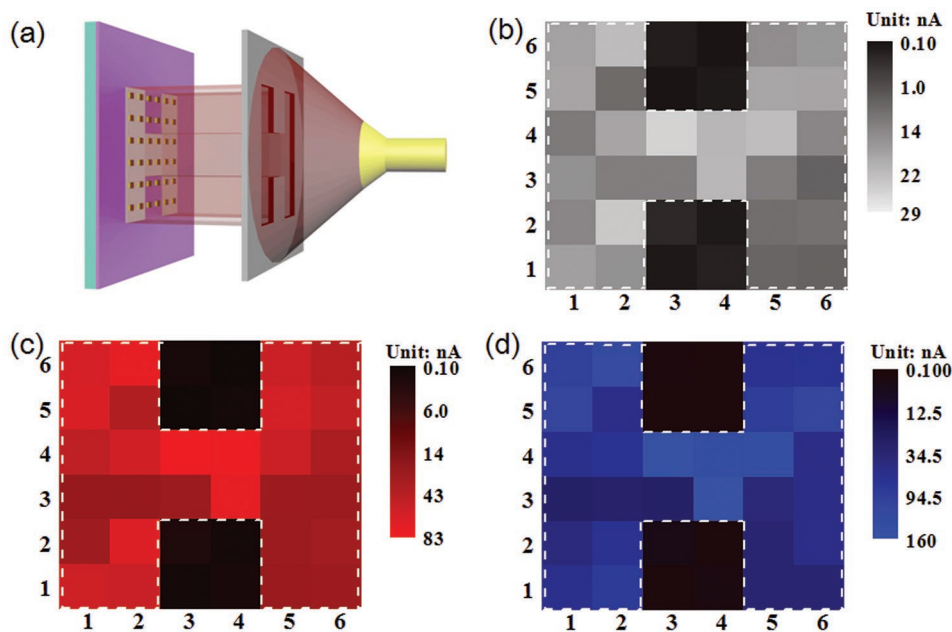


**Figure 7.** a) Schematic illustration of measurement setup for the perovskite photodetector arrays to realize visible light imaging sensing. The corresponding 2D current mapping of the photodetector arrays upon illumination with b) white light ( $350 \mu\text{W cm}^{-2}$ ), c) red light ( $650 \text{ nm}$ ,  $580 \mu\text{W cm}^{-2}$ ), and d) blue light ( $450 \text{ nm}$ ,  $1.45 \text{ mW cm}^{-2}$ ), respectively.

Finally, the capability of perovskite photodetector arrays to record visible light image was explored. To conduct the measurement, a lab-built metal mask with “H” pattern was placed between the homogenous illumination and the photodetector arrays. As schematically shown in **Figure 7a**, only light penetrated the hollow region of the mask can be projected on the pixels, whereas the rest of the pixels were kept in dark condition without illumination. The channel current of each pixel was measured and then incorporated into a 2D contrast map. Totally, three kinds of light sources including white light, illumination with wavelengths of 450 and 650 nm, were employed here. As observed in **Figure 7b–d**, for all three illuminations, only the pixels projected by the illumination displayed sizeable photocurrent, whereas the rest of the pixels showed weak channel current. Therefore, the shape of character “H” can be clearly identified in the contrast maps, implying the preliminary visible light imaging function of the perovskite photodetector arrays. The spatial resolution can be optimized by further miniaturizing the pixel devices. Given a response speed much faster than the time resolution of human eyes ( $\approx 42 \text{ ms}$ ), patterned perovskite-based visible light image sensors developed by the proposed technique are expected to have some important applications, e.g., artificial electronic eyes.<sup>[20]</sup>

### 3. Conclusions

In summary, by utilizing the hydrophobic nature of CVD-grown graphene films, we demonstrated the hydrophilic–hydrophobic surface-induced growth of high-quality perovskite films with well-patterned shapes, which was accomplished by a facile one-step spin-coating method. Based on such a technique, perovskite photodetector arrays were constructed, which displayed eminent

photoresponse characteristics with responsivity and specific detectivity of  $4.8 \text{ AW}^{-1}$  and  $4.2 \times 10^{12} \text{ Jones}$ , respectively, as well as small pixel-to-pixel variation. Furthermore, the good device performance enables the preliminary application of the photodetector arrays as an optical image sensor operating in the visible light region. Benefiting from the good compatibility with a variety of spin-coated perovskite materials, perovskite manufacturing processes, and substrates, the proposed technique is believed to have great potential for large-scale perovskite material-based integrated device and system applications.

### 4. Experimental Section

**Materials Preparation and Characterization:** Large-area continuous graphene films were synthesized at  $1000 \text{ }^\circ\text{C}$  on  $25 \mu\text{m}$  Cu foils utilizing a mixed gas of  $\text{CH}_4$  (40 sccm) and  $\text{H}_2$  (20 sccm) via a CVD method as reported in literatures.<sup>[46]</sup> The as-grown graphene films were transferred to other substrates through an extensively used PMMA-assisted wet transfer technique.<sup>[35]</sup> To prepare the perovskite precursor solution, 1 mmol  $\text{PbI}_2$  (Aldrich, 99%), 0.15 mmol  $\text{CsI}$  (Aldrich, 99.9%), and 0.85 mmol  $\text{FAI}$  (Aldrich, 99%) were sequentially added into a mixed solvent composed of 200  $\mu\text{L}$  dimethyl sulfoxide ( $>99.9\%$ ) and 800  $\mu\text{L}$   $N,N$ -dimethylformamide ( $>99.8\%$ ).<sup>[47]</sup> The as-mixed solution was then stirred at  $70 \text{ }^\circ\text{C}$  for 45 min to obtain a clear and transparent precursor solution prior to use.  $\text{FA}_{0.85}\text{Cs}_{0.15}\text{PbI}_3$  perovskite film was prepared by spin-coating 80  $\mu\text{L}$  of the above precursor solution onto a clean substrate at a speed of 600 rpm for 10 s and then 3000 rpm for 20 s, respectively. After thermal annealing at  $70 \text{ }^\circ\text{C}$  for 5 min and subsequent  $135 \text{ }^\circ\text{C}$  for 10 min, a black-brownish perovskite film was obtained on the substrate.

The morphology and composition of the as-obtained perovskite films were characterized by an FESEM (SIRION 200 FEG) and an XRD (Rigaku D/max-rB), respectively. The surface roughness of the films was observed by an AFM (Benyuan Nanotech Com., CSPM-4000). The contact angles of the perovskite precursor on graphene-coated and bare

SiO<sub>2</sub>/Si substrates were measured using an optical contact angle system (CAM, Dataphysics OCA25).

**Device Fabrication and Analysis:** To fabricate the perovskite photodetector arrays, 50 nm parallel Au electrodes arrays with 10 μm channel length were first deposited onto a clean SiO<sub>2</sub>/Si substrate through combined conventional photolithography, electron beam evaporation, and lift-off processes. Afterward, a CVD-graphene film was transferred atop the substrate, and then defined using another photolithography process followed by an oxygen plasma treatment to produce a patterned graphene film with 300 × 300 μm<sup>2</sup> exposed hydrophilic regions which intentionally overlap with the device channels. Finally, patterned perovskite films were grown followed the above preparation procedures and the residual graphene was removed by another oxygen plasma treatment.

Optoelectronic characterizations of the devices were conducted on a semiconductor characterization system (Keithley 4200-SCS), equipped with a monochromator (SP 2150, Princeton Co.). White light emitted from an optical microscope on the probe station and laser diodes with different wavelengths (405, 650, and 808 nm, Tanon UV-100) were used as the light sources. Before use, the light intensity of these light sources was carefully calibrated by a power meter (Thorlabs GmbH, PM 100D). For response speed measurement, the detector was illuminated by a high-frequency light irradiation emitted from a laser diode driven by a signal generator (Tektronix, 521TDS2022B), and the output photoresponse signal was recorded by an oscilloscope (Tektronix, DPO5104B). Unless other specified, all measurements were carried out at room temperature in ambient conditions.

## Supporting Information

Supporting Information is available from the Wiley Online Library or from the author.

## Acknowledgements

This work was supported by the Natural Science Foundation of China (NSFC, nos. 61575059, 61675062, 21501038), the Fundamental Research Funds for the Central Universities (JZ2018HGPD0275, JZ2018HGTA0220, JZ2018HGXC0001), and the National College Students' innovation and entrepreneurship training program (no. 201710359060).

## Conflict of Interest

The authors declare no conflict of interest.

## Keywords

graphene assisted, hydrophilic–hydrophobic surface, optical image sensor, patterned growth, perovskite film

Received: February 8, 2019

Revised: March 26, 2019

Published online: April 8, 2019

- 
- [1] B. Saporov, D. B. Mitzi, *Chem. Rev.* **2016**, *116*, 4558.  
[2] H. Zhou, Q. Chen, G. Li, S. Luo, T. B. Song, H. S. Duan, Z. Hong, J. You, Y. Liu, Y. Yang, *Science* **2014**, *345*, 542.  
[3] M. A. Green, A. Ho-Baillie, H. J. Snaith, *Nat. Photonics* **2014**, *8*, 506.  
[4] M. Grätzel, *Nat. Mater.* **2014**, *13*, 838.  
[5] H. Wang, D. H. Kim, *Chem. Soc. Rev.* **2017**, *46*, 5204.

- [6] C. Xie, P. You, Z. Liu, L. Li, F. Yan, *Light: Sci. Appl.* **2017**, *6*, e17023.  
[7] M. Ahmadi, T. Wu, B. Hu, *Adv. Mater.* **2017**, *29*, 1605242.  
[8] Y. Ling, Z. Yuan, Y. Tian, X. Wang, J. C. Wang, Y. Xin, K. Hanson, B. Ma, H. Gao, *Adv. Mater.* **2016**, *28*, 305.  
[9] W. Deng, X. Xu, X. Zhang, Y. Zhang, X. Jin, L. Wang, S.-T. Lee, J. Jie, *Adv. Funct. Mater.* **2016**, *26*, 4797.  
[10] H. Zhu, Y. Fu, F. Meng, X. Wu, Z. Gong, Q. Ding, M. V. Gustafsson, M. T. Trinh, S. Jin, X.-Y. Zhu, *Nat. Mater.* **2015**, *14*, 636.  
[11] Y. Zhao, K. Zhu, *Chem. Soc. Rev.* **2016**, *45*, 655.  
[12] Q. Chen, N. De Marco, Y. Yang, T. Bin Song, C. C. Chen, H. Zhao, Z. Hong, H. Zhou, Y. Yang, *Nano Today* **2015**, *10*, 355.  
[13] W. Tian, H. Zhou, L. Li, *Small* **2017**, *13*, 1702107.  
[14] J. Zhou, J. Huang, *Adv. Sci.* **2018**, *5*, 1700256.  
[15] Y. Wu, X. Zhang, H. Pan, W. Deng, X. Zhang, X. Zhang, J. Jie, *Sci. Rep.* **2013**, *3*, 3248.  
[16] C. Xie, Y. Wang, Z. X. Zhang, D. Wang, L. B. Luo, *Nano Today* **2018**, *19*, 41.  
[17] B. Jeong, I. Hwang, S. H. Cho, E. H. Kim, S. Cha, J. Lee, H. S. Kang, S. M. Cho, H. Choi, C. Park, *ACS Nano* **2016**, *10*, 9026.  
[18] N. Aristidou, I. Sanchez-Molina, T. Chotchuangchutchaval, M. Brown, L. Martinez, T. Rath, S. A. Haque, *Angew. Chem., Int. Ed.* **2015**, *54*, 8208.  
[19] D. Bryant, N. Aristidou, S. Pont, I. Sanchez-Molina, T. Chotchuangchutchaval, S. Wheeler, J. R. Durrant, S. A. Haque, *Energy Environ. Sci.* **2016**, *9*, 1655.  
[20] W. Deng, X. Zhang, L. Huang, X. Xu, L. Wang, J. Wang, Q. Shang, S. T. Lee, J. Jie, *Adv. Mater.* **2016**, *28*, 2201.  
[21] Q. Hu, H. Wu, J. Sun, D. Yan, Y. Gao, J. Yang, *Nanoscale* **2016**, *8*, 5350.  
[22] P. Liu, X. He, J. Ren, Q. Liao, J. Yao, H. Fu, *ACS Nano* **2017**, *11*, 5766.  
[23] J. Mao, W. E. I. Sha, H. Zhang, X. Ren, J. Zhuang, V. A. L. Roy, K. S. Wong, W. C. H. Choy, *Adv. Funct. Mater.* **2017**, *27*, 1606525.  
[24] L. Lee, J. Baek, K. S. Park, Y. E. Lee, N. K. Shrestha, M. M. Sung, *Nat. Commun.* **2017**, *8*, 15882.  
[25] W. Deng, L. Huang, X. Xu, X. Zhang, X. Jin, S.-T. Lee, J. Jie, *Nano Lett.* **2017**, *17*, 2482.  
[26] L. Gu, M. M. Tavakoli, D. Zhang, Q. Zhang, A. Waleed, Y. Xiao, K. H. Tsui, Y. Lin, L. Liao, J. Wang, Z. Fan, *Adv. Mater.* **2016**, *28*, 9713.  
[27] J. Feng, X. Yan, Y. Liu, H. Gao, Y. Wu, B. Su, L. Jiang, *Adv. Mater.* **2017**, *29*, 1605993.  
[28] G. Wang, D. Li, H.-C. Cheng, Y. Li, C.-Y. Chen, A. Yin, Z. Zhao, Z. Lin, H. Wu, Q. He, M. Ding, Y. Liu, Y. Huang, X. Duan, *Sci. Adv.* **2015**, *1*, e1500613.  
[29] X. Liu, L. Niu, C. Wu, C. Cong, H. Wang, Q. Zeng, H. He, Q. Fu, W. Fu, T. Yu, C. Jin, Z. Liu, T. C. Sum, *Adv. Sci.* **2016**, *3*, 1600137.  
[30] J. Feng, X. Yan, Y. Zhang, X. Wang, Y. Wu, B. Su, H. Fu, L. Jiang, *Adv. Mater.* **2016**, *28*, 3732.  
[31] J. Wu, J. Chen, Y. Zhang, Z. Xu, L. Zhao, T. Liu, D. Luo, W. Yang, K. Chen, Q. Hu, F. Ye, P. Wu, R. Zhu, Q. Gong, *Nano Lett.* **2017**, *17*, 3563.  
[32] W. Lee, J. Lee, H. Yun, J. Kim, J. Park, C. Choi, D. C. Kim, H. Seo, H. Lee, J. W. Yu, W. B. Lee, D.-H. Kim, *Adv. Mater.* **2017**, *29*, 1702902.  
[33] W. Wu, X. Wang, X. Han, Z. Yang, G. Gao, Y. Zhang, J. Hu, Y. Tan, A. Pan, C. Pan, *Adv. Mater.* **2019**, *31*, 1805913.  
[34] A. Kozbial, F. Zhou, Z. Li, H. Liu, L. Li, *Acc. Chem. Res.* **2016**, *49*, 2765.  
[35] J. W. Suk, A. Kitt, C. W. Magnuson, Y. Hao, S. Ahmed, J. An, A. K. Swan, B. B. Goldberg, R. S. Ruoff, *ACS Nano* **2011**, *5*, 6916.  
[36] F. X. Liang, J. Z. Wang, Z.-X. Zhang, Y. Y. Wang, Y. Gao, L. B. Luo, *Adv. Opt. Mater.* **2017**, *5*, 1700654.  
[37] D. Wu, Y. Wang, L. Zeng, C. Jia, E. Wu, T. Xu, Z. Shi, Y. Tian, X. Li, Y. H. Tsang, *ACS Photonics* **2018**, *5*, 3820.  
[38] Y. Shao, Z. Xiao, C. Bi, Y. Yuan, J. Huang, *Nat. Commun.* **2014**, *5*, 5784.

- [39] C. Xie, C. Mak, X. Tao, F. Yan, *Adv. Funct. Mater.* **2017**, *27*, 1603886.
- [40] M. Buscema, J. O. Island, D. J. Groenendijk, S. I. Blanter, G. A. Steele, H. S. J. van der Zant, A. Castellanos-Gomez, *Chem. Soc. Rev.* **2015**, *44*, 3691.
- [41] D. Kufer, I. Nikitskiy, T. Lasanta, G. Navickaite, F. H. L. Koppens, G. Konstantatos, *Adv. Mater.* **2015**, *27*, 176.
- [42] X. Li, M. Zhu, M. Du, Z. Lv, L. Zhang, Y. Li, Y. Yang, T. Yang, X. Li, K. Wang, H. Zhu, Y. Fang, *Small* **2016**, *12*, 595.
- [43] R. Zhuo, Y. Wang, D. Wu, Z. Lou, Z. Shi, T. Xu, J. Xu, Y. Tian, X. Li, *J. Mater. Chem. C* **2018**, *6*, 299.
- [44] F. Li, C. Ma, H. Wang, W. Hu, W. Yu, A. D. Sheikh, T. Wu, *Nat. Commun.* **2015**, *6*, 8238.
- [45] H. Deng, X. Yang, D. Dong, B. Li, D. Yang, S. Yuan, K. Qiao, Y. B. Cheng, J. Tang, H. Song, *Nano Lett.* **2015**, *15*, 7963.
- [46] L. H. Zeng, M. Z. Wang, H. Hu, B. Nie, Y. Q. Yu, C.-Y. Wu, L. Wang, J. G. Hu, C. Xie, F. X. Liang, L. B. Luo, *ACS Appl. Mater. Interfaces* **2013**, *5*, 9362.
- [47] Z. X. Zhang, L. H. Zeng, X. W. Tong, Y. Gao, C. Xie, Y. H. Tsang, L. B. Luo, Y. C. Wu, *J. Phys. Chem. Lett.* **2018**, *9*, 1185.